ELSEVIER

Journal of Fluids and Structures 25 (2009) 969–990

JOURNAL OF FLUIDS AND STRUCTURES

www.elsevier.com/locate/jfs

Wake structures and vortex-induced vibrations of a long flexible cylinder—Part 1: Dynamic response

F.J. Huera-Huarte[a,*,1], P.W. Bearman[b]

[a]*Department of Mechanical Engineering, Universitat Rovira i Virgili, 43007 Tarragona, Spain*
[b]*Department of Aeronautics, Imperial College London, SW7 2AZ London, UK*

Received 29 September 2008; accepted 24 March 2009
Available online 26 May 2009

Abstract

Results showing the dynamic response of a vertical long flexible cylinder vibrating at low mode numbers are presented in this paper. The model had an external diameter of 16 mm and a total length of 1.5 m giving an aspect ratio of about 94, with Reynolds numbers between 1200 and 12 000. Only the lower 40% of its length was exposed to the water current in the flume and applied top tensions varied from 15 to 110 N giving fundamental natural frequencies in the range from 3.0 to 7.1 Hz. Reduced velocities based on the fundamental natural frequency up to 16 were reached. The mass ratio was 1.8 and the combined mass–damping parameter about 0.05. Cross-flow and in-line amplitudes, x–y trajectories and phase synchronisation, dominant frequencies and modal amplitudes are reported. Cross-flow amplitudes up to 0.7 diameters and in-line amplitudes over 0.2 were observed with dominant frequencies given by a Strouhal number of 0.16.

Keywords: Vortex-induced vibration; Dynamic response; Phase synchronisation; Long flexible circular cylinders

1. Introduction

In the area of vortex-induced vibration (VIV) of cylinders, the vast majority of research efforts in the past have been focused on the study of flexibly mounted rigid bodies, with one degree of freedom (dof), the transverse motion. Well-known reviews on this topic are Bearman (1984), Sarpkaya (2004) and Williamson and Govardhan (2004). The dynamic response of rigid cylindrical structures is well documented and the effects of combined mass–damping characteristics on the maximum attainable amplitudes, especially in low mass and damping systems, are major concerns in offshore engineering.

Although differences between the responses of flexibly mounted rigid cylinders with 1 or 2 degrees of freedom have been found, many of the features documented for 1 dof cases are still valid for 2 dof systems, at least for low mass–damping systems with mass ratios higher than 6. These recent investigations enhance the understanding of fluid–structure interactions but what it is not completely clear is if these studies have direct relevance to offshore engineering applications dealing with long flexible cylinders, especially those prone to vibrate at high mode numbers.

*Corresponding author.
E-mail address: francisco.huera@urv.cat (F.J. Huera-Huarte).
[1]Present address: Graduate Aeronautical Laboratories, California Institute of Technology, Pasadena, CA 91125, USA.

0889-9746/$ - see front matter © 2009 Elsevier Ltd. All rights reserved.
doi:10.1016/j.jfluidstructs.2009.03.007

Most of the engineering applications in which VIV is a problem involve flexible bluff bodies with the same mass, damping and mechanical characteristics in-line and cross-flow, which imply complex motions. Several investigations such as the ones reported by Vandiver and Marcollo (2003), Chaplin et al. (2005b), Trim et al. (2005) and Lie and Kaasen (2006), have been conducted to investigate VIV under these conditions. The paradigm of one or two dof rigid cylinder VIV behaviour being a valid hypothesis to predict the response of flexible cylinders, is still a major concern.

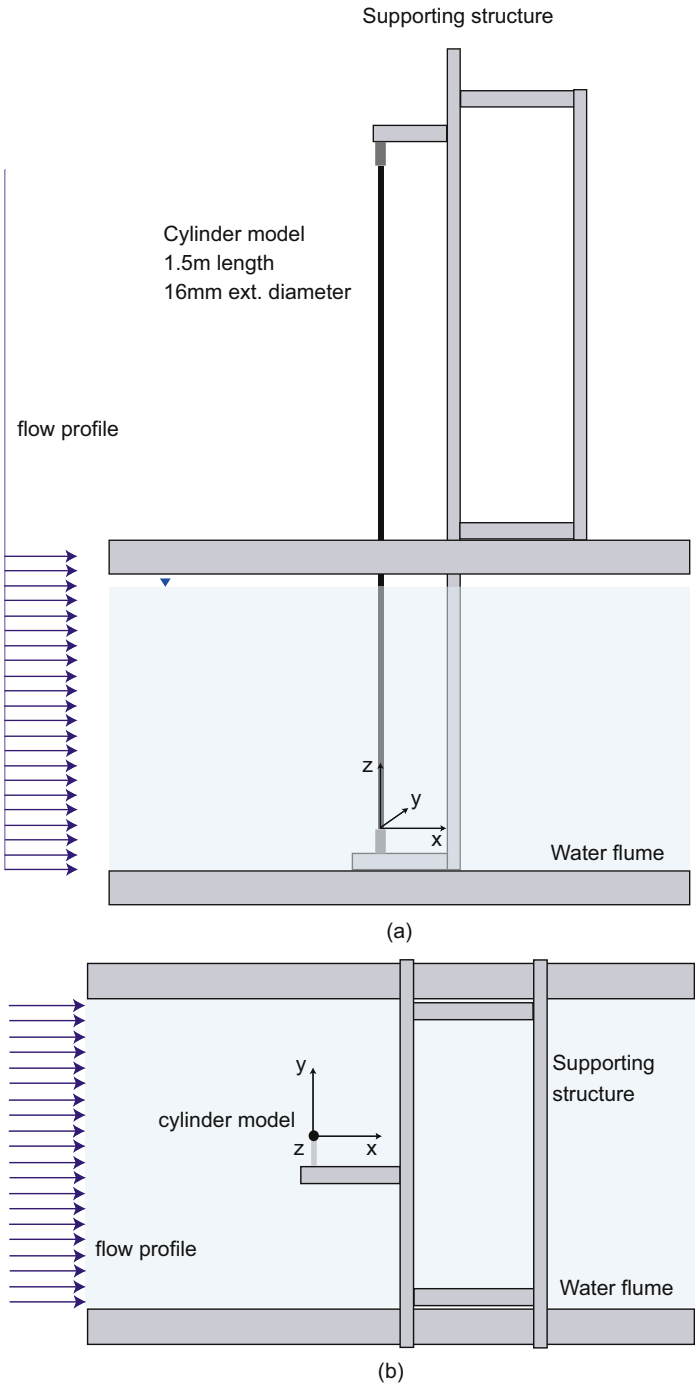

Fig. 1. Layout of the experiment. (a) Side view. (b) Top view.

Looking to recent investigations, it seems that there are still many discrepancies between predictions from computational codes and even between the empirical methods (Chaplin et al., 2005a). Important differences in the dynamic response of flexible bodies arise due to the intrinsic nature of the body, its capacity to vibrate at high mode numbers and the complex added mass and hydrodynamic damping distributions while in motion. The response, both in-line and transverse to the flow, and the fluid forces exerted on the body are now mode dependent, adding extra complexity. Recent experiments carried out in May 2003 on a long flexible cylinder at the Delta Flume (Chaplin et al., 2005b), showed the behaviour of a flexible circular cylinder with a mass ratio of about 3 and an aspect ratio of 400, responding multi-modally with responses up to the 8th cross-flow and the 14th in-line structural modes. According to the data presented by Jauvtis and Williamson (2004), at mass ratios lower than 6 with cylinders in two degree of freedom motion, one should expect amplitudes over 1.5 diameters in what has been called the super-upper branch. The Delta Flume experiments showed a strong lock-in behaviour in which the model responded with monotonically increasing amplitudes that reached similar maxima inside clearly defined mode dependent reduced velocity regions. The dynamic response was closely scrutinised and the main observations revealed important differences from the typical response of rigid circular cylinders. Ratios between the cross-flow and the in-line motion in the range from 2 to 4 were presented in Huera-Huarte (2006), showing agreement with those suggested by Trim et al. (2005). These ratios are a common characteristic in flexible cylinder response in front of the high ratios reported in Jauvtis and Williamson (2003).

2. Experimental details

The experiments were performed in a water channel at the Department of Aeronautics of Imperial College London. The test section is 0.6×0.75 m with a total length exceeding 8 m. The maximum water depth can be varied up to about 0.65 m, and the pumping system is able to generate currents up to 0.75 m/s at the maximum water depth.

2.1. The cylinder model

The model, with the same damping, mass and natural frequencies in both directions, allows the study of vortex-induced motion of a continuous (or multi degree of freedom) system, in which different responding amplitudes are found at different heights along the length of the model. The set-up, Figs. 1(a) and (b), consisted of a supporting structure and a long flexible circular cylinder instrumented with strain gauges along its length. The design of the model was based on that described in Chaplin et al. (2005b) and used at the Delta Flume in 2003. The 1.5 m long circular cylinder had a 6 mm diameter aluminium core with 15 mm diameter aluminium diaphragms attached to it with cyanoacrylate glue. This skeleton structure was covered with a transparent flexible PVC skin, providing an external diameter of 16 mm and an aspect ratio (length/diameter) of about 94. The PVC skin provided a smooth external surface

Table 1
Main parameters.

Experiment parameters			
External diameter	D	m	0.016
Length	L	m	1.5
Aspect ratio	L/D	–	93.75
Submerged length	L_s	m	0.585
Flexural stiffness	EI	$\mathrm{N\,m^2}$	6.04
Axial stiffness	EA	MN	1.84
Top tension	T_t	N	<110
Flow speed	V	m/s	<0.75
Reynolds number	Re	–	1200–12 000
Mass	m	kg/m	0.362
Submerged weight	w_s	N/m	2.7
Mass ratio	m^*	–	1.8
Fund. natural freq.	f_1	Hz	3.0–7.1
Damping ratio	ζ	% ζ_c	1.77

as well as protection for the instrumentation, not allowing the water inside the hollow parts of the model. The total mass of riser, including the instrumentation cables, was 0.362 kg/m and its submerged weight was 2.7 N/m. The flexural stiffness was kept very low, 6.04 N m^2 and the mass ratio (ratio of structural mass to displaced fluid mass) was approximately 1.8.

A very stiff aluminium structure was designed to secure the ends of the model (Fig. 1(a)). The model was attached vertically to the supporting structure through universal joints at both ends, with the possibility of changing the applied top tension through a spring system, therefore allowing changes in its natural frequencies. A total of five top tensions (15, 35, 60, 85 and 110 N) were tested. The natural frequencies in water of the first structural mode of vibration are shown in the last column of Table 2 for each top tension. These natural frequencies were obtained in modal tests but they have also been calculated with a finite element code which solves the eigenvalue problem of an Euler–Bernoulli

Table 2
Summary of tests.

Initial top tension T_t (N)	Symbol	Number of runs	f_1 (Hz)
15	□	19	3.0
35	◇	23	4.5
60	*	20	5.6
85	+	21	6.5
110	○	20	7.1

First column indicates the initial top tension applied to the model, the second column indicates the symbol used in all the figures and the third indicates the number of runs conducted at each top tension.

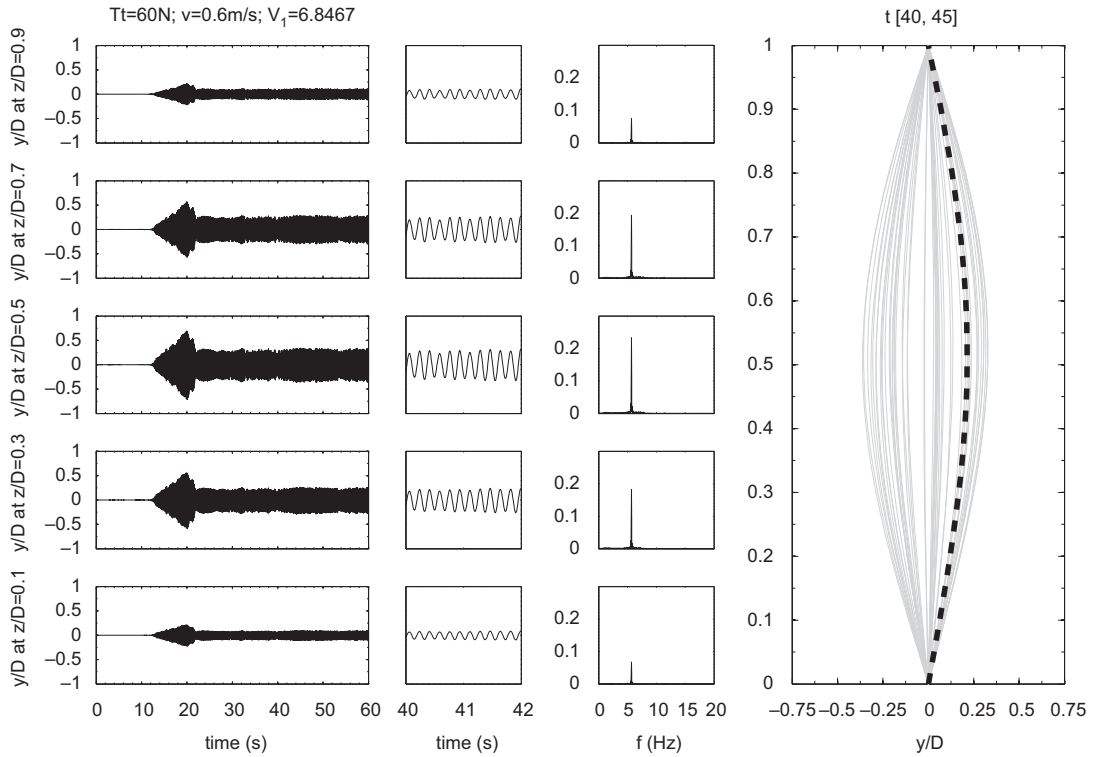

Fig. 2. Example of test: $V = 0.60$ m/s, $T_t = 60$ N, Re $= 8400$, $V_1 = 6.85$. First column shows the instantaneous non-dimensional cross-flow displacements for the whole run, at each position along the length of the model in which a strain gauge station was installed. The second column shows an enlargement of 2 s inside the test. The third column shows the spectra of each signal. The fourth column shows the cross-flow deflections; solid lines represent motion every $\frac{1}{10}$th of a second inside the interval $t[40, 45]$, and the dashed line is used for the root mean square value of the motion in the selected time window.

beam [see Huera-Huarte (2006) for more details] and very good agreement was observed. The structural modal damping ratios were obtained from decay tests in air. The model was forced to vibrate at a constant amplitude in a certain mode and then the forcing was stopped. The damping ratios were obtained by analysing the exponential decay of amplitudes for each top tension tested. The values, as a percentage of critical damping, were found to be in the range from 1.45% to 1.95%, with a mean value of $\zeta = 1.77\%$. The model was situated more than 15 diameters upstream of the supporting structure in order not to have any influence of that in the wake of the cylinder.

The apparatus was installed in the water flume exposing the lower 40% of the model to the current. In an experiment such as this one it is desired to have large shedding frequencies and a model with low natural frequencies, in order to be able to excite the cylinder over the widest possible range of reduced velocities and mode numbers. High shedding frequencies are obtained with high flow speeds and small model diameters, however, there are limitations imposed by the facility regarding the maximum attainable flow speed, and there are also limitations in the minimum external diameter of the model, as instrumentation needs to be embedded in it. The length of the cylinder model is a critical design parameter as its natural frequencies are inversely proportional to the square of the length. This means that high aspect ratio (L/D) models in water tunnels able to deliver high flow speeds are the best combination. As the length of the models is increased, the required size of the facilities also increases. A solution in order to keep high aspect ratios in relatively small facilities is to use reduced water coverages. This was first done by Chaplin et al. (2005b) and it was seen how a reduced water coverage was able to excite high modes. In that experimental campaign, several experiments were conducted in order to find the main differences in the response caused by different water coverages. It was seen how over a certain threshold, which was less than 30%, the excited modes in the response did not vary. Hydrodynamic damping and added mass are considerably reduced in the upper part of the model, but it was verified that the responses were still not remarkably altered, by carrying out some tests in which the upper part of the model was not surrounded by water. The excited modes and the response were still the same and small changes appeared only in the mean in-line

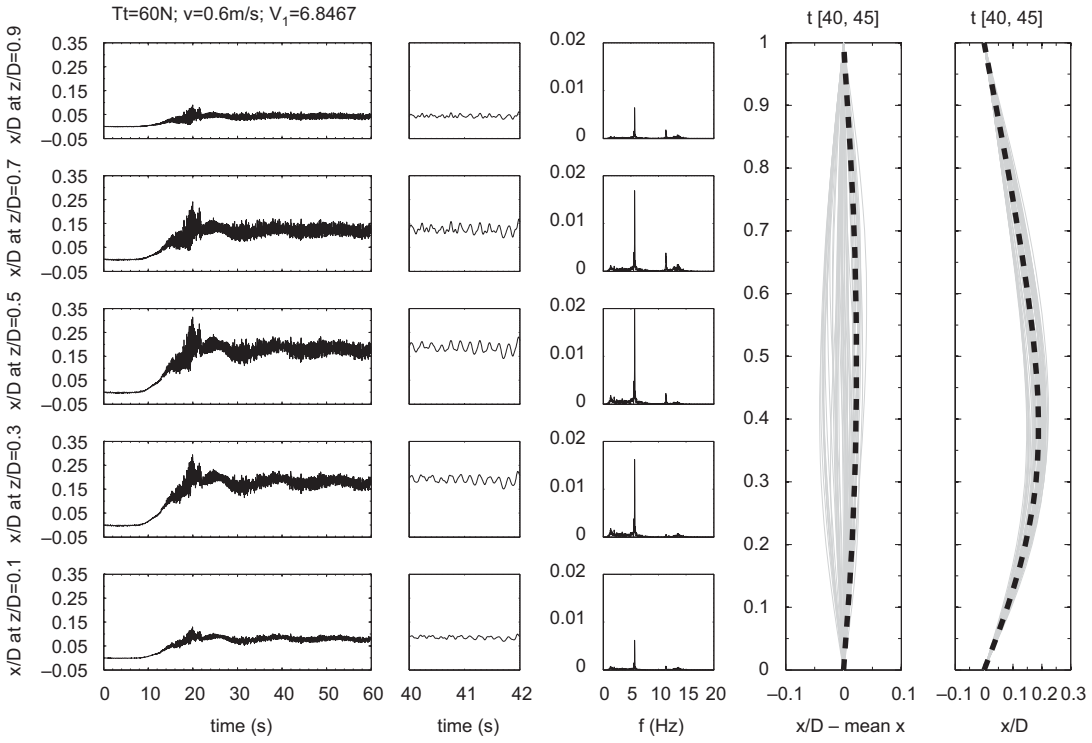

Fig. 3. Example of test: $V = 0.60\,\mathrm{m/s}$, $T_t = 60\,\mathrm{N}$, $\mathrm{Re} = 8400$, $V_1 = 6.85$. First column shows the instantaneous non-dimensional in-line displacement for the whole run, at each position along the length of the model in which a strain gauge station was installed. The second column shows an enlargement of 2 s inside the test. The third column shows the spectra of each signal. The fourth and fifth columns show the in-line motion after removing and without removing the mean in-line deflection, respectively; solid lines represent motion every $\frac{1}{10}$th of a second inside the interval $t[40, 45]$; the dashed line in the fourth column is used for the root mean square value and the dashed line in the fifth column represents the mean deflection of the motion in the selected time window.

deflections as the mean drag acts only in the lower part of the model, and the maximum mean in-line deflection does not occur at the mid point of the model anymore. Details can be found in Huera-Huarte (2006).

For each of the top tensions the flow speed was varied between 0.1 and 0.75 m/s in increments of 0.05 m/s, producing a uniform velocity profile acting on the lower 40% of the model, with Reynolds numbers varying from about 1400 to 12 000. Each run, lasting a total of 60 s, was started from still water allowing enough time for the initial flow transient to die away. Table 1 presents the main parameters of the experimental arrangement. As the preparation of each run required changes to parameters in the acquisition system, the water tank pumping system control and sometimes the tension applied to the model, more than 5 min were allowed between each run, enough for the vorticity to be damped away from one run to the next.

In offshore applications it is common to find arrangements of single or several long flexible circular structures in non-uniform flows such as sheared or stepped flows. Stepped or abrupt shear flows in the ocean can lead to situations in which large currents are combined with regions with no current or very low current at different positions along the structures.

2.2. Instrumentation

The cylinder model was equipped with five strain gauge measurement stations distributed every 300 mm starting at 150 mm from the ends. Each one of the measurement stations was formed by two half Wheatstone bridges measuring

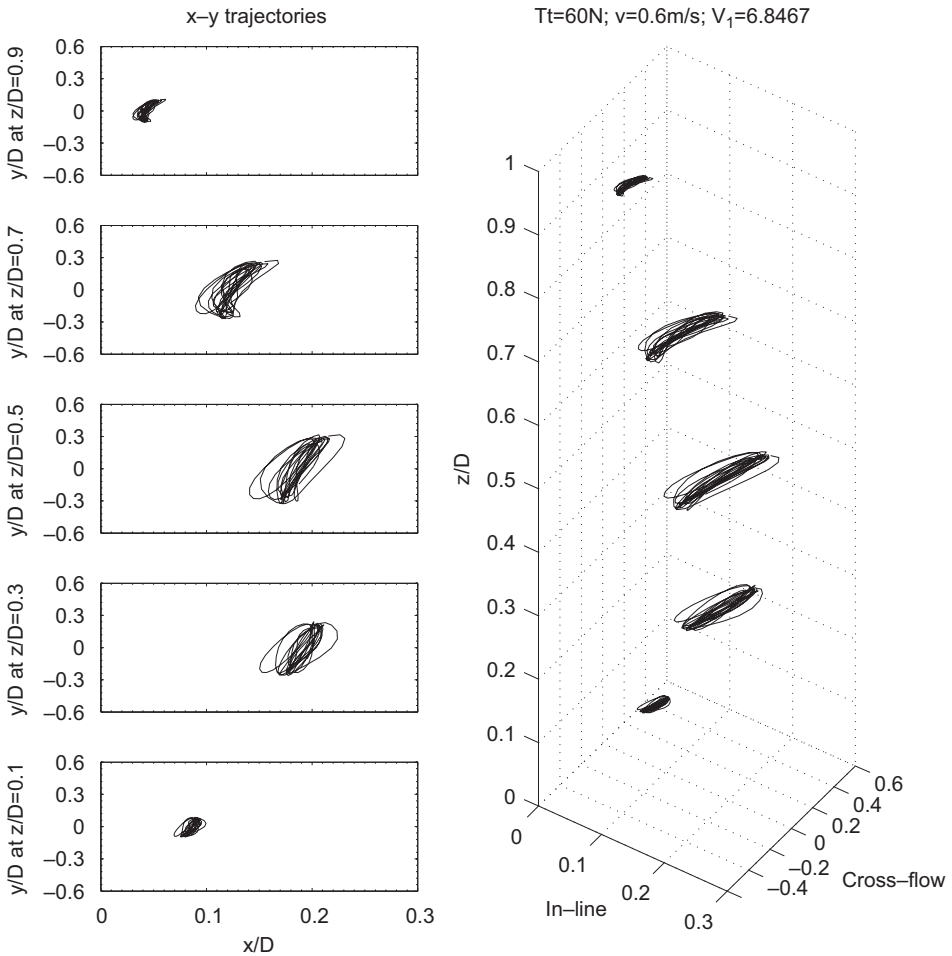

Fig. 4. Example of test: $V = 0.60\,\mathrm{m/s}$, $T_t = 60\,\mathrm{N}$, $\mathrm{Re} = 8400$, $V_1 = 6.85$. Left hand side depicts the trajectories at each one of the measurement stations from the 40th to the 42nd second. Right hand side shows an alternative representation of the motion of the model along its length.

the bending simultaneously in the direction aligned with the flow (in-line), and in the direction transverse to the flow (cross-flow). This arrangement of the instrumentation was suitable for measurements up to the fifth structural mode of vibration, well above the highest expected mode for these experiments. Displacements were computed from bending, by calculating the double spatial integral of the curvatures. The in-line and transverse curvatures as a function of time t and the position along the axis of the cylinder are

$$c_x(z,t)=\frac{\partial^2 x(z,t)}{\partial z^2},\quad c_y(z,t)=\frac{\partial^2 y(z,t)}{\partial z^2}, \tag{1}$$

where x are y are the in-line and transverse motions, respectively, which can be calculated as follows:

$$x(z,t)=\int_o^L\int_o^L\frac{\partial^2 x(z,t)}{\partial z^2}\,\mathrm{d}z\,\mathrm{d}z,\quad y(z,t)=\int_o^L\int_o^L\frac{\partial^2 y(z,t)}{\partial z^2}\,\mathrm{d}z\,\mathrm{d}z. \tag{2}$$

The boundary conditions for these expressions are those of a pin ended beam that has zero displacements and zero curvatures at the ends

$$\begin{aligned} &x(z,t)=y(z,t)=0,\quad z=0,L\ \ \forall t,\\ &\frac{\partial^2 x(z,t)}{\partial z^2}=\frac{\partial^2 y(z,t)}{\partial z^2}=0,\quad z=0,L\ \ \forall t. \end{aligned} \tag{3}$$

Strain gauges were successful in showing the high mode structural response of a long flexible cylinder responding to vortex shedding, in a previous experimental investigation (Chaplin et al., 2005b). In this case, in order to verify that calibrations and the strain gauge measurements were correct, they were compared against independent laser sensor displacement measurements, showing very good agreement.

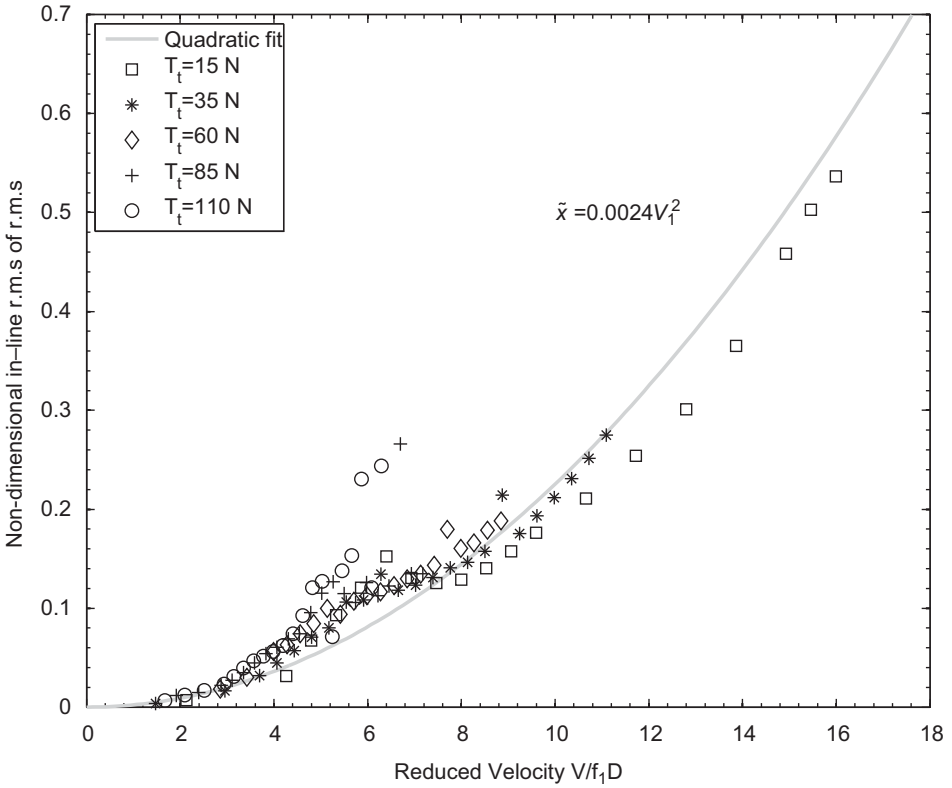

Fig. 5. Root mean square (r.m.s.) of the in-line motion ($\tilde{x}/D$) as defined by Eq. (5) versus reduced velocity V_1. The solid line is the best quadratic fit for the present work data, given by $\tilde{x}=0.0024V_1^2$.

3. Results

In this section the dynamic response of the model is analysed by studying amplitudes, frequencies, phase relations between x and y motions and modal amplitudes for each data set. The data are presented according to the different sets of applied top tensions, presented in Table 2. A total of more than 100 tests were carried out, producing a large set of data.

As already stated in Section 2.1, for each run, a time window in which the response was found to be steady, was selected to perform the data analysis. Even though the top tension increases with drag, the initial values have been used for the data analysis and for the calculation of the natural frequencies due to the fact that the tension was not measured during the course of a run. In the following section, the amplitudes are nondimensionalised by the diameter and the reduced velocity is based on the fundamental natural frequency in water:

$$V_1 = \frac{V}{f_1 D}. \tag{4}$$

3.1. Dynamic response

Figs. 2–4 show results for a case in which the applied top tension was 60 N, the flow speed was 0.6 m/s, giving a Reynolds number of about 8400, and the reduced velocity was 6.85. This test is used as an example to illustrate the data analysis carried out on every run.

In Fig. 2 the instantaneous cross-flow amplitudes at each position where a strain gauge was fixed, are shown in columns 1 and 2. All runs were started from still water and after a few seconds (12 in this case) the pumping system was turned on, so the water started to flow in the flume. The time window for the analysis was chosen for each test assuring that this transient period was avoided. In the test shown, from 22 s onwards, the response seems to have reached a more

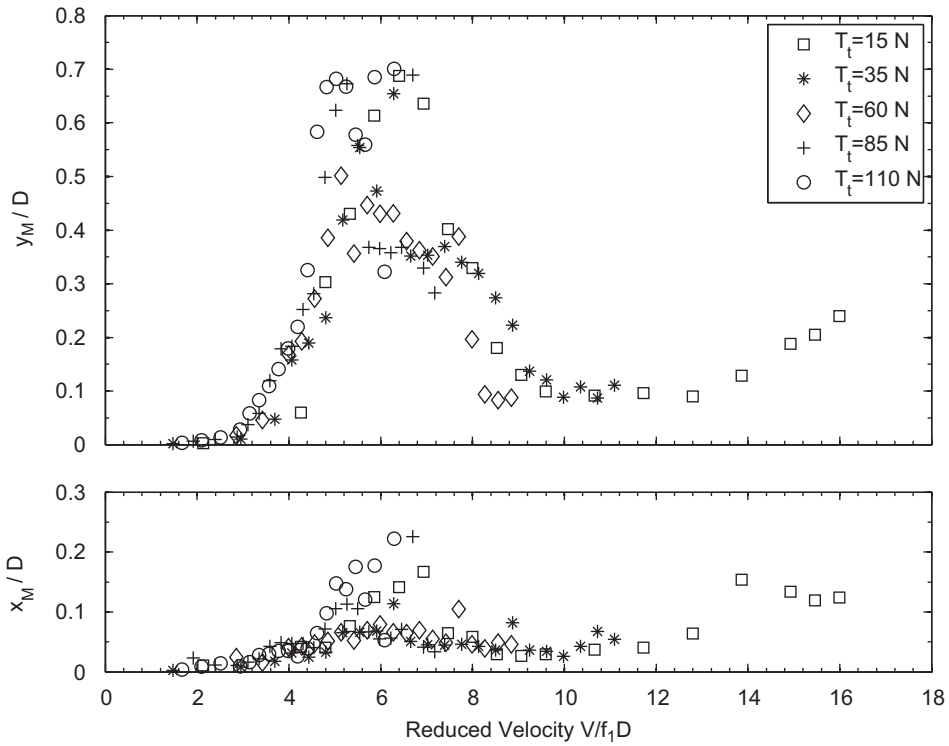

Fig. 6. Maxima of in-line (x_M/D) and cross-flow displacements (y_M/D).

or less constant amplitude. The third column in Fig. 2 shows spectra of each one of the signals in column 1. In all cases clear peaks can be identified and in some more than one peak was observed, depending on how close the natural frequency of each mode was to the vortex shedding frequency. The last column in Fig. 2 shows the deflections along the length of the model every $\frac{1}{10}$th of a second between the 40th and the 45th seconds with solid lines, and the root-mean-square (r.m.s.) value with a dashed line.

Fig. 3, for the in-line response is structured in the same fashion as Fig. 2. The first two columns are used to show the time series of the in-line deflections and the third column shows the spectra. In the fourth column the displacements along the length, after removing the mean deflection, are shown every $\frac{1}{10}$th of a second inside the interval $[40, 45]$ with solid lines, together with the root mean square with a dashed line. The last column shows the in-line motions and the mean deflection with a dashed line. A 3-D representation of the trajectories along the length of the model is shown in Fig. 4 for the same example test. The trajectories show several vortex shedding cycles from the 40th second to the 45th. A similar data analysis was applied to each of the more than 100 runs to produce Figs. 5–9 of this section.

The root-mean-square of the in-line motion for each test is shown in Fig. 5. It has been calculated as the temporal r.m.s. of the spatial (spanwise) r.m.s. for each instant in time of the in-line motion. It is given by

$$\widetilde{x} = \sqrt{\frac{1}{s}\sum_{i=1}^{s}\left[\frac{1}{N}\sum_{j=1}^{N} x_{ji}^2(z,t)\right]}, \tag{5}$$

where s is the number of time samples in the selected time window for the analysis and N is the number of nodes at which a measurement station was located. The drag force on the model increases as the square of the flow speed, as does the in-line deflection. Hence the data in the figure follow roughly the second order equation $\widetilde{x} = 0.0024V_1^2$, depicted by the solid line in the figure.

The in-line motion of the flexible body is also analysed by removing the mean deflection from the overall in-line displacements. The maximum non-dimensional cross-flow (Y_M/D) and in-line (X_M/D) amplitudes caused by

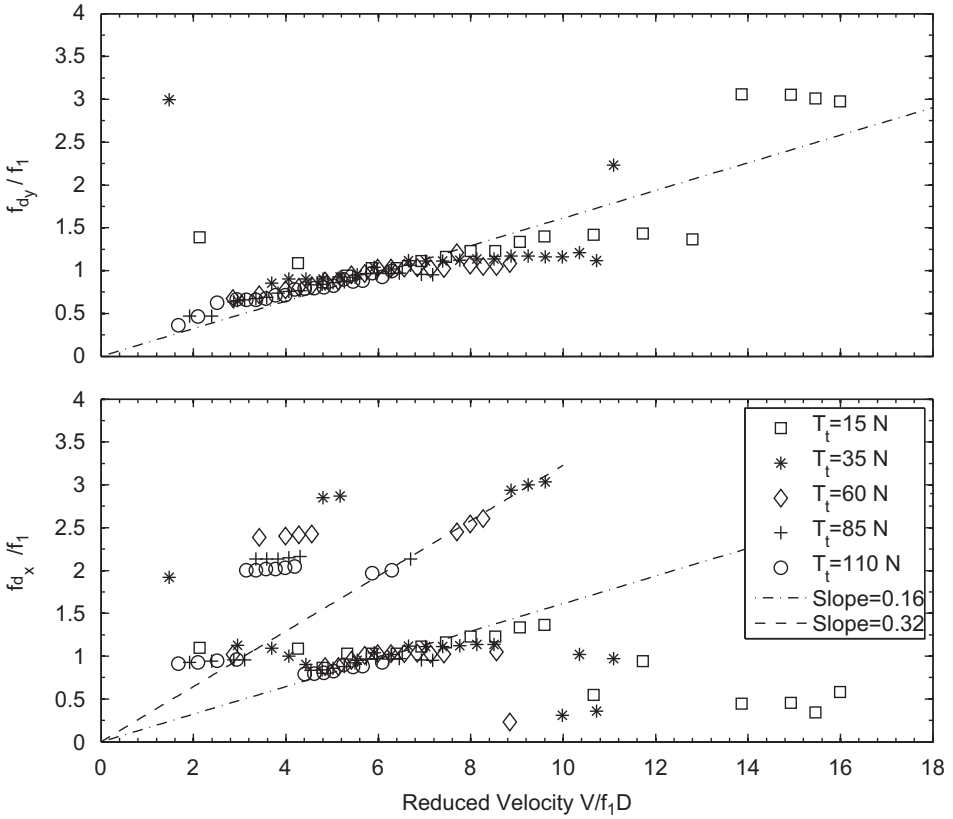

Fig. 7. Normalised responding cross-flow f_{d_y}/f_1 and in-line f_{d_x}/f_1 frequencies as a function of V_1. Linear fits of equation $f_{d_y}/f_1 = 0.16V_1$ and $f_{d_y}/f_1 = 0.32V_1$ are presented with a dot-dashed line and with a dashed line, respectively.

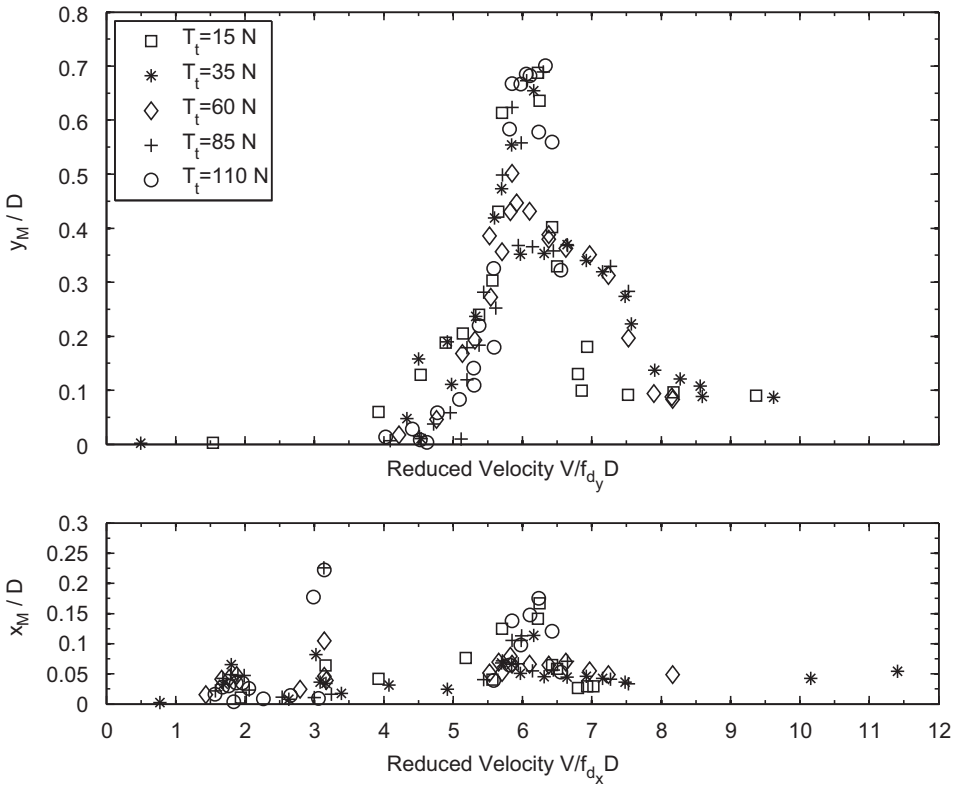

Fig. 8. Maxima of in-line (x/D) and cross-flow displacements (y/D) versus reduced velocity based on the dominant in-line (f_{d_y}) and cross-flow frequencies (f_{d_x}).

vortex-shedding are plotted in Fig. 6 versus the reduced velocity V_1. Initial, upper and lower branches of response are evident in the cross-flow results. It is also clear that instead of the desynchronisation branch, the build-up of the second mode of the response is observed. If higher reduced velocities could have been achieved, the lock-in region of the second mode would have been observed, as reported previously by Chaplin et al. (2005b). The in-line response shows the same characteristics with the same branches but they are not as evident as in the cross-flow case. The maximum cross-flow displacement occurs at a reduced velocity in the range 5–7 with a peak value about 0.7 diameters. In the same reduced velocity range, the in-line amplitudes exceed 0.15 diameters reaching a peak value over 0.2 at a reduced velocity around 6. In the build up of the second mode branch, amplitudes increase monotonically both for the cross-flow and in-line motions. The ratio transverse to in-line amplitude varies between 4 and 6 in most of the cases, whilst in previous two-degree-of- freedom rigid body studies practically no in-line motion was observed. This fact introduces very important differences in the dynamic response and it has obviously practical implications in offshore design, as well as it could mean differences in the vortex dynamics as pointed out by Jeon and Gharib (2001) in their forced vibration experiments. In Section 4 a compilation of previous data obtained by several researchers in experiments involving rigid body motions of one and two degrees of freedom and in flexible cylinders, is presented and discussed against the present work data.

Normalised dominant frequencies are plotted in Fig. 7. The frequencies have been found by carrying out Fourier analysis of the modal contributions. The ratio of the dominant frequency in the cross-flow response to the fundamental natural frequency in water, f_{d_y}/f_1, matches that given by the frequency of the vortex shedding and it is about 1 for V_1 between 5 and 11, that is when the response did not have any contribution from the second mode. A linear fit with slope 0.16 is presented in the figure. Exactly the same slope was found in the Delta Flume campaign (Huera-Huarte, 2006). If the frequency of vortex shedding is assumed to be equal to the dominant frequency in the response, the Strouhal number can be inferred from the data and in this case it is 0.16. The normalised in-line frequencies are shown in the lower plot of the figure, where two linear fits are presented with slopes of 0.16 and 0.32. The oscillating part of the drag is characterised by frequencies which are twice those of the cross-flow response, but in order to have an in-line response at a frequency twice the cross-flow, the flow must be able to generate excitations at the frequency of the second mode.

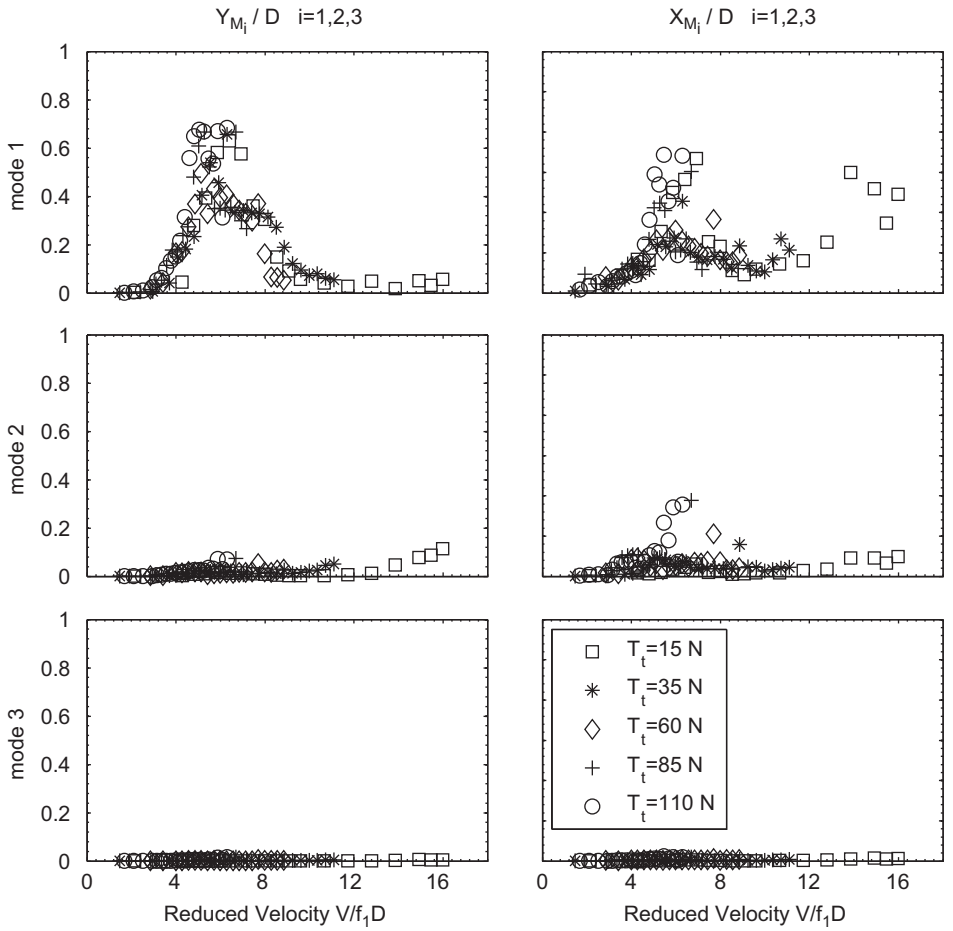

Fig. 9. In-line (x_{M_i}/D) and cross-flow (y_{M_i}/D) modal contributions of modes up to the third. The modal decomposition leading to the modal contributions has been computed assuming sinusoidal mode shapes as described in Eq. (7).

This happened weakly only in a very few cases because of the low maximum attainable flow speed in the flume. At the maximum flow velocity (0.75 m/s), the frequency of the exciting cross-flow force is $f_s = S(U/D) \simeq 7.5$ Hz and the frequency of the exciting in-line force should be $2f_s \simeq 15$ Hz. The frequency of the second mode was only below 15 Hz for top tensions less than 60 N. This is why in these experiments the in-line and cross-flow responding modes and frequencies were the same, except in a few cases in which the applied top tension was the lowest and the flow speeds were the highest.

By using the reduced velocity based on the dominant responding frequency (V_d), one obtains the collapse of data shown in Fig. 8. For the cross-flow case, the initial, upper and lower branches are still clear but all the responses concentrate around values of $V_{d_y} \simeq 1/S = 6.25$, in the range from 4 to 9. The in-line response is characterised now by three clear regions in V_{d_x} as reported by previous authors (Wooton et al., 1974; Jauvtis and Williamson, 2003). The first region showed symmetric shedding of vortices whilst the second showed asymmetric shedding. The maxima inside each of the three in-line regions were reported at reduced velocities $<1/2S$, $\simeq 1/2S$ and $\simeq 1/S$, and as can be seen from the present data, in Fig. 8 they occur at 1.75, 3.1 and 6.25, respectively.

Fig. 9 confirms that the response was found in almost all the test cases to be in the 1st cross-flow and in-line modes. Cross-flow contributions of the 2nd mode were only observed at the lower top tensions, for reduced velocities higher than 11. In-line contributions from the second mode are observed in some of the higher tension cases for reduced velocities around 6 and for all cases with reduced velocities higher than 11. No responses dominated purely by the second mode were observed; that would require frequencies of about 17 Hz at the highest tension cases, and the flow speed was not high enough to generate them. Regarding the third mode, there is no contribution to the overall response at all. The values shown in the figures are the maxima of each mode contribution to the overall response. These values

have been obtained from the measured displacements, by assuming sinusoidal mode shapes. Modal analysis is based on the fact that the riser response can be expressed in matrix form as a linear combination of its modes.

$$\mathbf{y}(z,t) = \mathbf{\Phi}(z)\mathbf{y}_M(t), \quad \mathbf{x}(z,t) = \mathbf{\Phi}(z)\mathbf{x}_M(t), \tag{6}$$

where $\mathbf{\Phi} = [\phi_1, \phi_2, \ldots, \phi_n]$ is the displacement modal-shape matrix and its column components are the non-dimensional displacement mode shapes normalised to be 1 at its maximum. $\mathbf{y}(z,t) = [y_1(z_1,t), y_2(z_2,t), \ldots, y_n(z_n,t)]$ and $\mathbf{x}(z,t) = [x_1(z_1,t), x_2(z_2,t), \ldots, x_n(z_n,t)]$ are the measured displacements matrices, where each row vector y_i, x_i is the time series of the measured displacement at a certain height (z_i) along the length of the model, at which a strain gauge station was located. $\mathbf{y}_M(t)$ and $\mathbf{x}_M(t)$ are the modal contribution matrices, containing the time series of each mode's contribution to the overall response as the row vectors $\mathbf{y}_M(t) = [y_{M_1}(t), y_{M_2}(t), \ldots, y_{M_n}(t)]$ and $\mathbf{x}_M(t) = [x_{M_1}(t), x_{M_2}(t), \ldots, x_{M_n}(t)]$,

$$\mathbf{y}_M(t) = \mathbf{\Phi}^{-1}(z)\mathbf{y}(z,t), \quad \mathbf{x}_M(t) = \Phi^{-1}(z)\mathbf{x}(z,t). \tag{7}$$

The mode shapes are normalised to 1 and bold letters indicate matrices or vectors. It has to be noted that for the in-line case, the static deformation or mean deflected shape has been previously removed, therefore only the dynamic part of the in-line motions are used in the modal decomposition.

3.2. $x-y$ Motion synchronisation

The motions at certain planes perpendicular to the axis of the cylinder are plotted to give the trajectories as shown in the example in Fig. 4. As the in-line and cross-flow motion are coupled, a complete analysis of the motion of the model requires a study of the amplitudes, frequencies and phases and how they are related to each other. The concept of

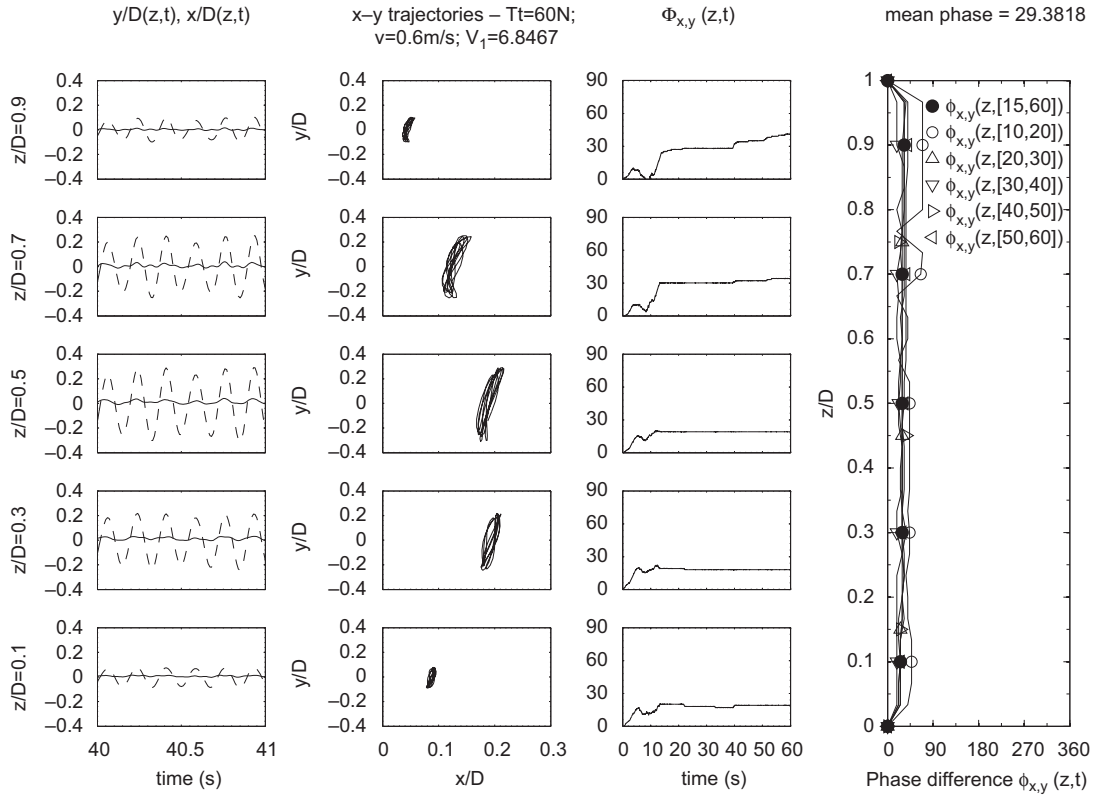

Fig. 10. Example of test: $V = 0.60\,\mathrm{m/s}$, $T_t = 60\,\mathrm{N}$, $\mathrm{Re} = 8400$, $V_1 = 6.85$. In the first column the time series of the cross-flow (dashed line) and in-line (solid line) displacements are shown for 2 s of the run. The second column shows the trajectories. In the third column the time series of the phase differences $\phi_{x,y}(z_i,t)$ are plotted. Finally, the last column depicts the phase differences $\phi_{x,y}^{t_i,t_{i+1}}(z_i)$ calculated for different time intervals.

synchronisation has been widely used to study oscillators in dynamical systems, and it is used here to investigate the interdependence of the in-line and the cross-flow motions. A methodology has been developed to analyse the data, based on the analysis of instantaneous phase and frequency of a signal. The objective is to determine in which parts of each run the in-line and the cross-flow motions are synchronised and in which parts the $x-y$ motions are independent. Indeed, it is very important to clarify that the concept of phase difference only makes sense when synchronisation occurs. Another important fact is that the notion of phase synchronisation only implies a relation between the phases of the signal while the amplitudes could remain unrelated. For the purpose of properly detecting the interrelation between signals, the concept of the analytical signal must be introduced and applied to the displacement signals:

$$\xi(z_i,t) = s(z_i,t) + \mathrm{i}s_H(z_i,t) = A(z_i,t)\mathrm{e}^{\mathrm{i}\phi(z_i,t)}. \tag{8}$$

Here $s(z_i,t)$ represents either the in-line $x(z,t)$ or cross-flow motion $y(z,t)$ at a height z_i along the axis of the model and $s_H(z_i,t)$ is the Hilbert transform of $s(z_i,t)$. The instantaneous amplitude $A(z_i,t)$ and the instantaneous phase $\phi(z_i,t)$ of $s(z_i,t)$ are then uniquely defined. The analytical function can be applied to any signal but it has physical meaning only in narrow banded signals such as the ones in this work (Pikovsky et al., 2001). The instantaneous frequency of the signal is

$$\Omega_x(z_i,t) = \frac{\mathrm{d}\phi_x(z_i,t)}{\mathrm{d}t}, \quad \Omega_y(z_i,t) = \frac{\mathrm{d}\phi_y(z_i,t)}{\mathrm{d}t}. \tag{9}$$

If the signals are not too noisy, a straightforward way to investigate the existence of synchronisation is to compute the instantaneous phases of each signal and then to calculate the instantaneous phase difference between them as

$$\phi_{x,y}(z_i,t) = n\phi_x(z_i,t) - m\phi_y(z_i,t), \tag{10}$$

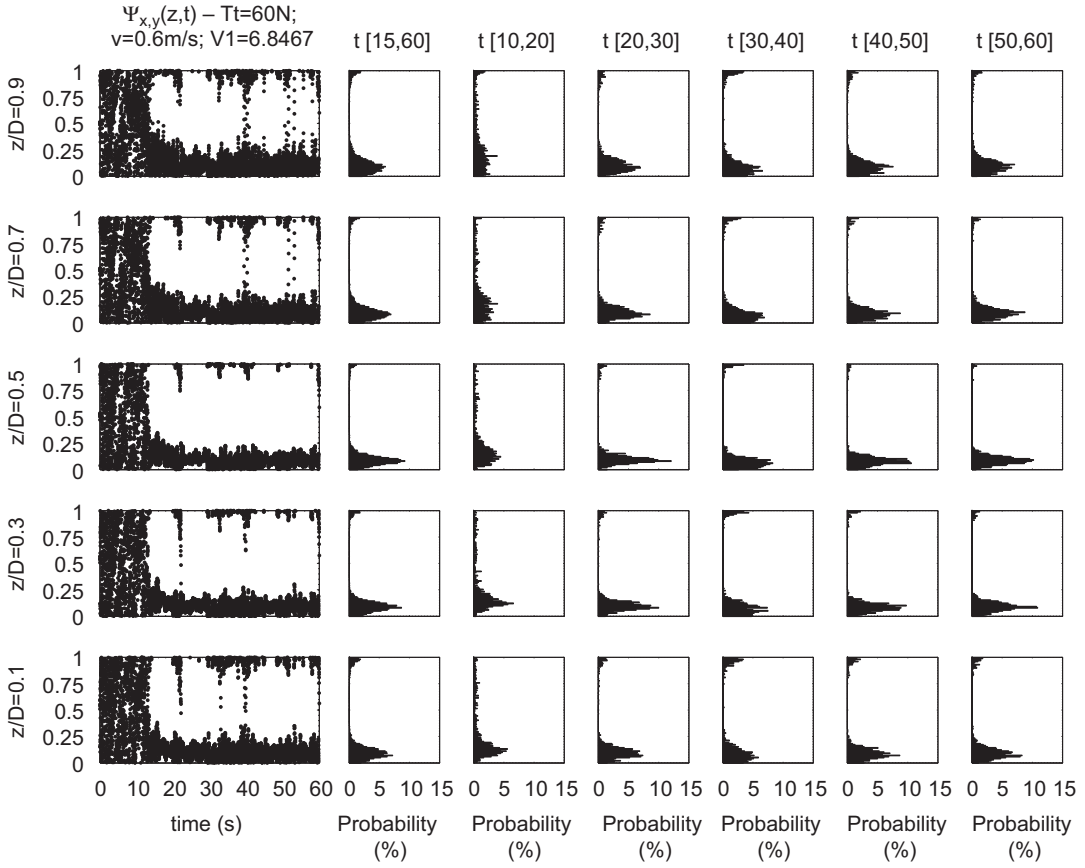

Fig. 11. Example of test: $V = 0.60\,\mathrm{m/s}$, $T_t = 60\,\mathrm{N}$, $\mathrm{Re} = 8400$, $V_1 = 6.85$. In the first column the time series of the cyclic phase difference $\Psi_{x,y}(z_i,t)$ is shown for the whole run. The other five columns show the synchrograms calculated according to the different time intervals.

where n and m are two coefficients related to the ratio of instantaneous frequencies such as $\Omega_x(z_i,t)/\Omega_y(z_i,t)=n/m$. By plotting the phase difference in time, synchronisation occurs when the phase difference remains constant, i.e. when the time series of the phase difference exhibits a plateau in time. Unfortunately, for experimental signals noise is unavoidable and the instantaneous phase difference can result in numerous phase shifts caused by the noise that masks the real results. Hence, other techniques must be used to complement the identification of synchronisation. In this work a statistical method has been applied for this purpose, and it has been extended to all the tests. The methodology is based on the computation of phase histograms (synchrograms) which will allow us to obtain the phase difference for each run. Fig. 10 shows the phase differences for the test presented as an example in Figs. 2–4. The first column shows the in-line (solid line) and cross-flow (dashed line) motion for the 40th second at each strain gauge. The second column shows the x–y trajectories in the same time window. In column three the instantaneous phase difference between the two signals $\phi_{x,y}(z_i,t)$ is depicted for the whole run at each height (z_i). These are obtained by applying the standard phase difference study and it is evident that $\phi_{x,y}$ remains constant from the 12th second onwards and synchronisation is clear. This conclusion is reinforced by looking to the plot in the last column of Fig. 10, which shows the phase at each measurement station for the different time intervals indicated in the legend. The data in this column is the result of plotting the statistical data shown in Fig. 11. Phase differences in Fig. 16 have been computed for 6 different time intervals: $\Delta t_{15}=[15,60]$, $\Delta t_{10}=[10,20]$, $\Delta t_{20}=[20,30]$, $\Delta t_{30}=[30,40]$, $\Delta t_{40}=[40,50]$ and $\Delta t_{50}=[50,60]$. Note that the first 10 s have been avoided because of the transient due to the fact that all the runs where started in still water. In the case presented in Figs. 10 and 11, the signals are not too noisy and strongly narrow banded with clearly defined frequency peaks, hence synchronisation can be determined directly from the instantaneous phase. It remains practically constant and there are no phase shifts from 13th second. In other cases, where synchronisation occurs only in parts of the run or where there are phase shifts, the standard method based only on the analysis of instantaneous phase

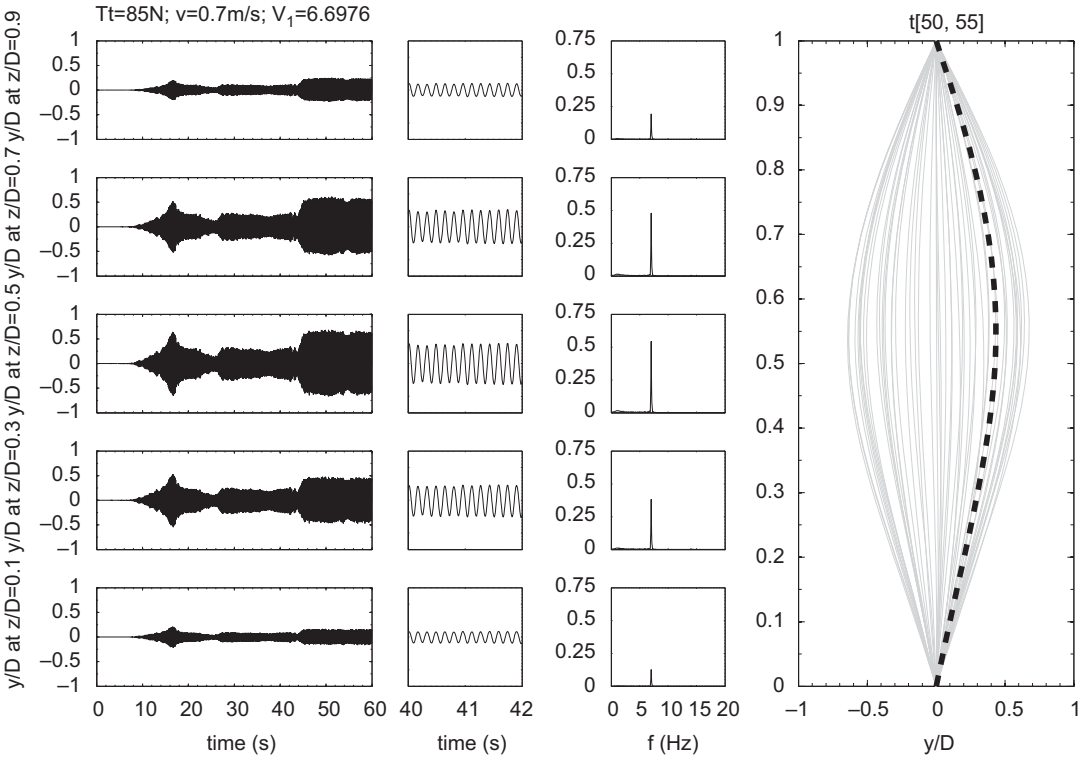

Fig. 12. Example of test: $V=0.70\,\mathrm{m/s}$, $T_t=85\,\mathrm{N}$, $\mathrm{Re}=9800$, $V_1=6.7$. First column shows the instantaneous non-dimensional cross-flow displacement for the whole run, at a position along the length of the model in which a strain gauge station was installed. The second column shows an enlargement of 2 s inside the test. The third column shows the spectra of each signal. The fourth column shows the cross-flow deflections; solid lines represent motion every $\frac{1}{10}$th of a second inside the interval $t[50,55]$, and the dashed line is used for the root mean square value of the motion in the selected time window.

difference plateaus, does not always yield to good results and it needs to be complemented with the statistical analysis proposed here.

The results from the statistical analysis methodology applied to all the tests support the conclusions obtained by the analysis of the time series of the phase difference $\phi_{x,y}(z_i,t)$. In the example shown, it can be seen how there are practically no differences when calculating the phase in the different time intervals as can be seen in Fig. 11. The statistical methodology is based on the calculation of the cyclic phase difference,

$$\Psi_{x,y}(z_i,t)=\frac{1}{2\pi}[\phi_{x,y}\bmod(2\pi)] \tag{11}$$

and the frequency distribution $\chi_{x,y}(z_i,t)$ of each cyclic phase, also called synchrogram. The synchrograms can be analysed by finding the best Gaussian fit to the data, according to

$$\chi_{x,y}(z_i,t)=\frac{1}{\sigma\sqrt{2\pi}}\mathrm{e}^{-\frac{1}{2}[\Psi_{x,y}(z_i,t)-\mu/\sigma]^2}, \tag{12}$$

where μ is the mean and σ is the standard deviation of the Gaussian distribution. A unimodal distribution with a small amplitude peak (σ) indicates synchronisation and the mean (μ) of the distribution indicates the value of the phase difference. $\chi_{x,y}(z_i,t)$ has been computed for the six different time intervals Δt_{15}, Δt_{10}, Δt_{20}, Δt_{30}, Δt_{40} and Δt_{50}, so the existence of synchronisation and the occurrence of phase shifts in time, can be studied for each run. Fig. 11 shows the synchrograms obtained from $\chi_{x,y}(z_i,t)$ for each position along the length of the model and for the six different time intervals. The first column shows the time series of the cyclic phase difference $\Psi_{x,y}(z_i,t)$ at each z_i. The phase angle in these plots is normalised to 2π as given by Eq. (11), hence 0.5 in this plot indicates 180° or π radians and so on. The

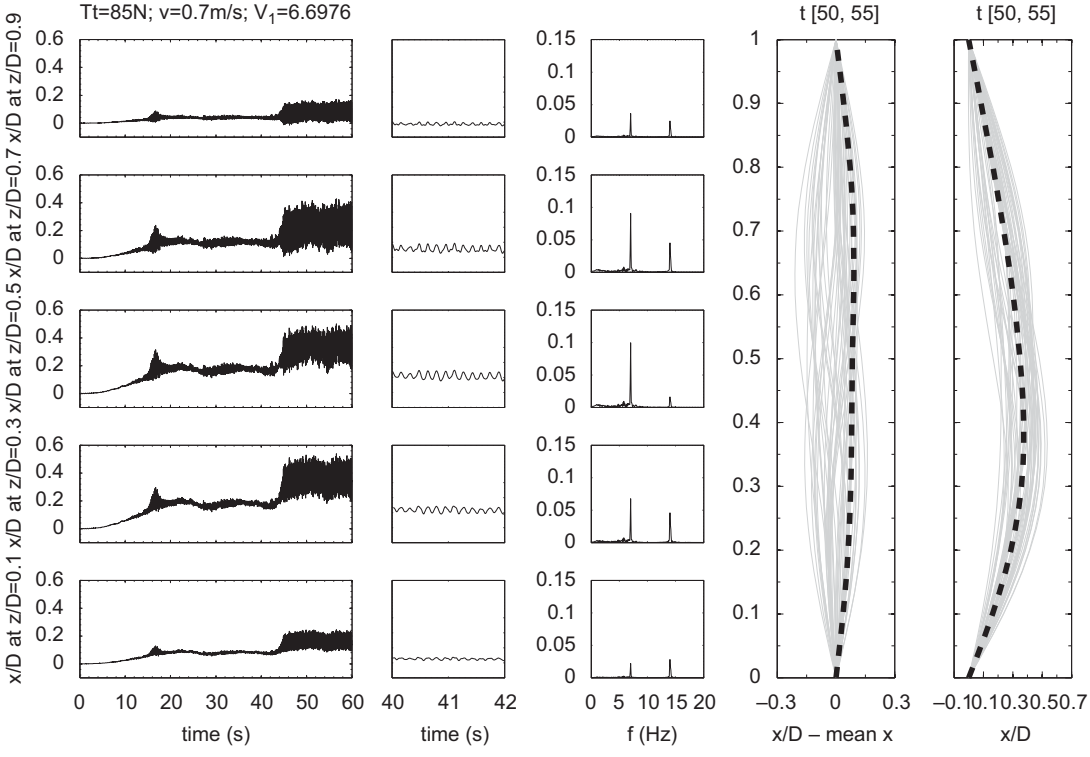

Fig. 13. Example of test: $V=0.70\,\mathrm{m/s}$, $T_t=85\,\mathrm{N}$, $\mathrm{Re}=9800$, $V_1=6.7$. First column shows the instantaneous non-dimensional in-line displacement for the whole run, at a position along the length of the model in which a strain gauge station was installed. The second column shows an enlargement of 2 s inside the test. The third column shows the spectra of each signal. The fourth and fifth columns show the in-line motion after removing and without removing the mean in-line deflection, respectively; solid lines represent motion every $\frac{1}{10}$th of a second inside the interval $t[50,55]$; the dashed line in the fourth column is used for the root mean square value and the dashed line in the fifth column represents the mean deflection of the motion in the selected time window.

second column shows the probability density function or synchrogram $\chi_{x,y}(z_i, t)$ computed in the interval Δt_{15}. The rest of the columns present the synchrograms computed in the time intervals Δt_{10}, Δt_{20}, Δt_{30}, Δt_{40} and Δt_{50}, respectively. By considering the first or the second column in Fig. 11 it is clear that synchronisation exists from the 15th second onwards, with a phase difference of about 30°. In fact, all the synchrograms are unimodal with clear peaks giving the phase difference between the x and the y motion. Only the synchrograms corresponding to the time interval Δt_{10} at $z = 1.35$ and 1.05 show a distribution which does not seem to be Gaussian. The plot of the phase found at each height from the synchrograms appears in the last column of Fig. 10. Each of the symbols represent the phase in the different time intervals. This example run was characterised by the absence of amplitude modulation, and a very narrow banded spectra, both in-line (Fig. 3) and cross-flow (Fig. 2). But not all the cases were like this and in those runs the methodology to investigate synchronisation has proved to be extremely useful compared to the simpler study of the time series of the phase difference.

Figs. 12–16 illustrate a case for a top tension of 85 N, a flow speed of 0.7 m/s, a reduced velocity of 6.7 and a Reynolds number of 9800 in which strong modulation and phase shifts are observed. Fig. 12 shows how the transverse motion seems to be steady between the 27th and the 42nd second, and suddenly it changes to another steady state but at a considerably higher amplitude until the end of the run. The same happens with the in-line amplitude as can be seen in Fig. 13. Fig. 14 shows the trajectories at the different heights along the axis of the cylinder. Dark lines are the plots of the trajectories in the time interval $t[50, 52]$ and grey lines are used for the interval $t[30, 32]$. Differences are also very

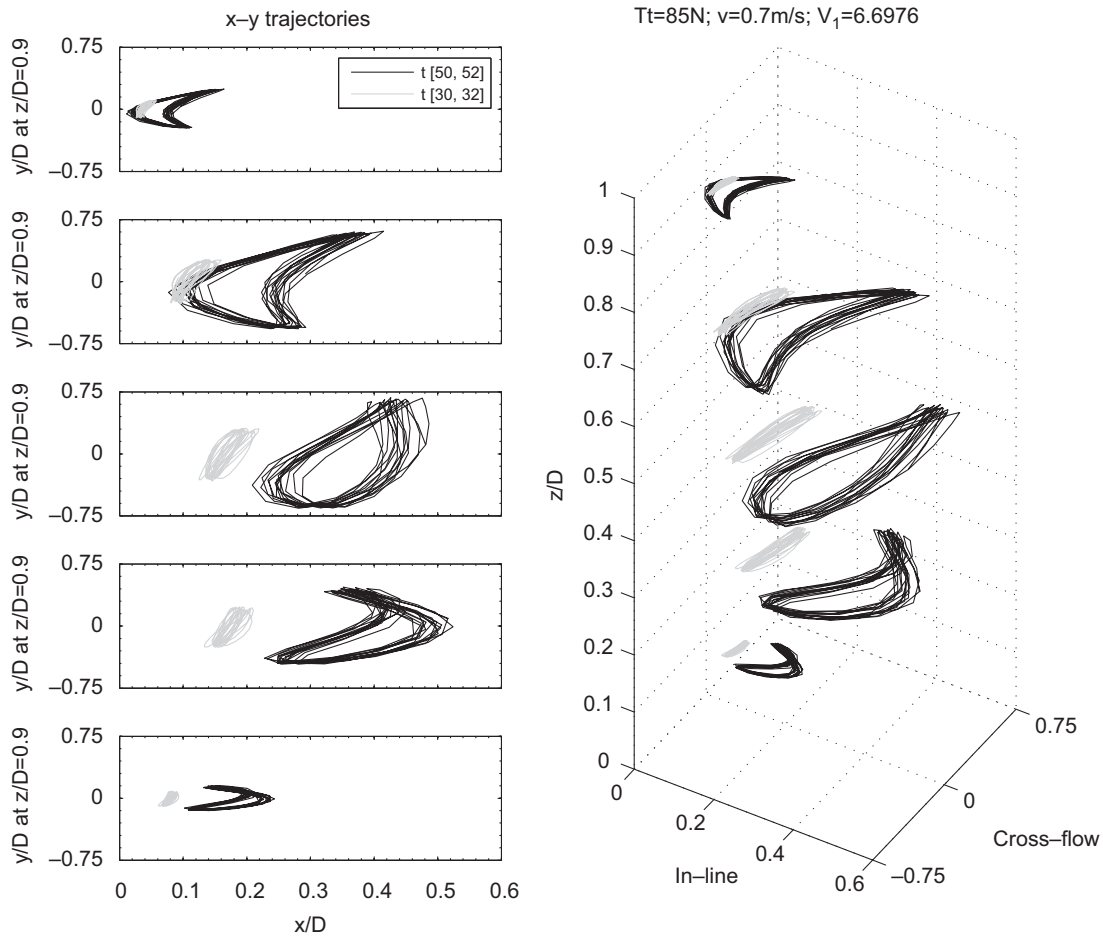

Fig. 14. Example of test: $V = 0.70$ m/s, $T_t = 85$ N, Re = 9800, $V_1 = 6.7$. First column depicts lissajous figures showing the trajectories at each one of the measurement stations with dark lines in the interval $t[50, 52]$ and with grey lines in $t[30, 32]$. The second column shows a 3D representation of the motion of the model.

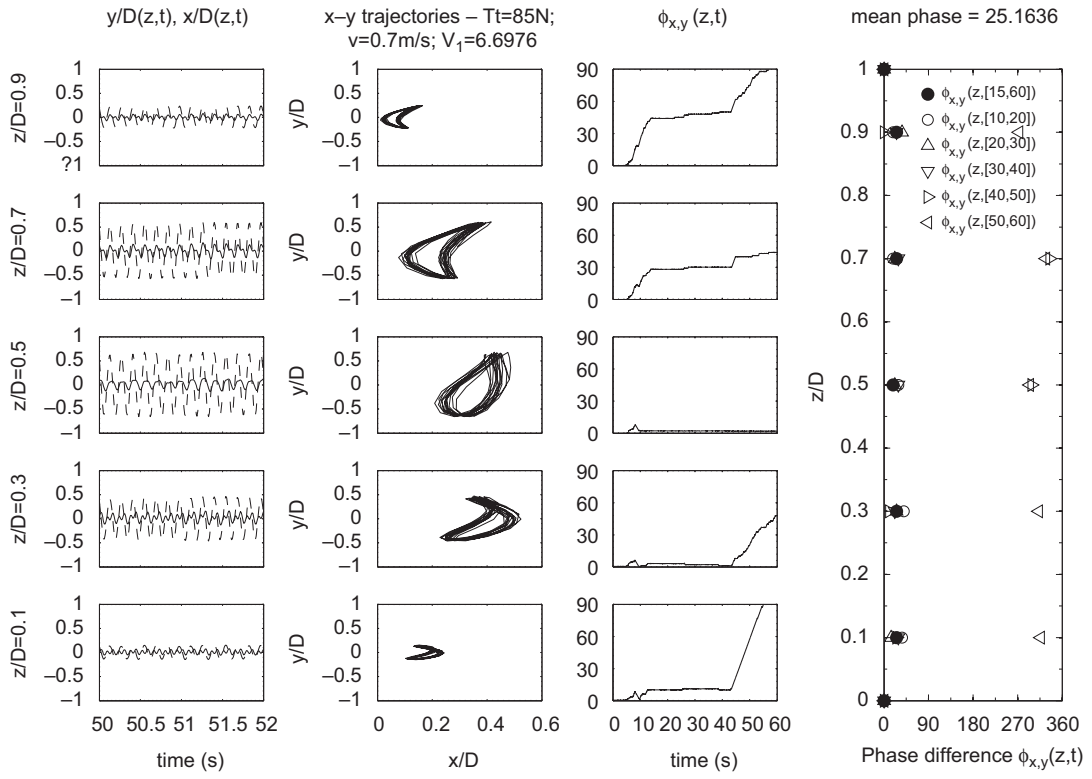

Fig. 15. Example of test: $V = 0.70\,\mathrm{m/s}$, $T_t = 85\,\mathrm{N}$, $\mathrm{Re} = 9800$, $V_1 = 6.7$. In the first column the time series of the cross-flow (dashed line) and in-line (solid line) displacements are shown for 2 s of the run. The second column shows the trajectories. In the third column the time series of the phase differences $\phi_{x,y}(z_i, t)$ are plotted. Finally, the last column depicts the phase differences $\phi_{x,y}^{t_i,t_{i+1}}(z_i)$ calculated for different time intervals.

clear in this plot. The synchronisation analysis in Fig. 15 reveals a plateau in the phase plot and the absence of synchronisation from the 42nd second onwards. It seems that in this case, without the supporting information provided by the synchrograms in Fig. 16, the phase differences in the third column of Fig. 15 imply the non-existence of synchronisation from the 42nd second on, when in fact synchronisation takes place at two different phases before and after the 42nd second of the run. Columns 3–5 in Fig. 16 indicate synchronisation in the time intervals Δt_{10}, Δt_{20} and Δt_{30} with a phase around 30°–45°. The last two columns give clear synchronisation at $z_i = 0.75\,\mathrm{m}$ with a phase of 315° but it is not so obvious at the other heights were $\chi_{x,y}(z_i, t)$ resembles a uniform rather than Gaussian distribution. This result can also be seen in the last column of Fig. 15, obtained from the synchrograms in Fig. 16,where the phases remain at a value around 30°–45° over the length of the model in the intervals Δt_{10}, Δt_{20} and Δt_{30} but has a value of about 315° (−45°) in the intervals Δt_{40} and Δt_{50}. In order to quantify the degree of synchronisation, a synchronisation index SI has been defined as the percentage of time in which synchronisation is observed, and this is obtained from the synchrograms of each time interval at a certain position along the length of the model. This methodology provides a very powerful technique to study synchronisation and phase interdependence in VIV and it can be implemented relatively easily to large sets of data.

The results of applying this method to all the runs are shown in Fig. 17. The first two plots show the cross-flow and in-line amplitudes against the reduced velocity as in Fig. 6 in order to relate them to phases and SI. The third plot shows the synchronisation index (SI) which clearly indicates the degree to which synchronisation is found. The last plot in the figure shows the phase differences in the interval Δt_{15} at the mid point of the model $z = 0.75$ m, $\phi_{x,y}^{15,60}(z_i)$, for all the tests in which synchronisation was found, that is for $\mathrm{SI} > 0$. The three small plots give the lissajous figures for theoretical $x - y$ motions with phase differences of 90°, 315° and 45° assuming that cross-flow and in-line frequencies are the same. By observing the SI plot it can be concluded that synchronisation only takes place for reduced velocities $V_1 \geqslant 3.8$. A SI of 100% is found only for V_1 between 4 and 9.5. Synchronisations with SI equal to 20%, 40% and 60% are found in some runs to fall inside the initial branch and also in some of the runs for the lower branch. The beginning of the second

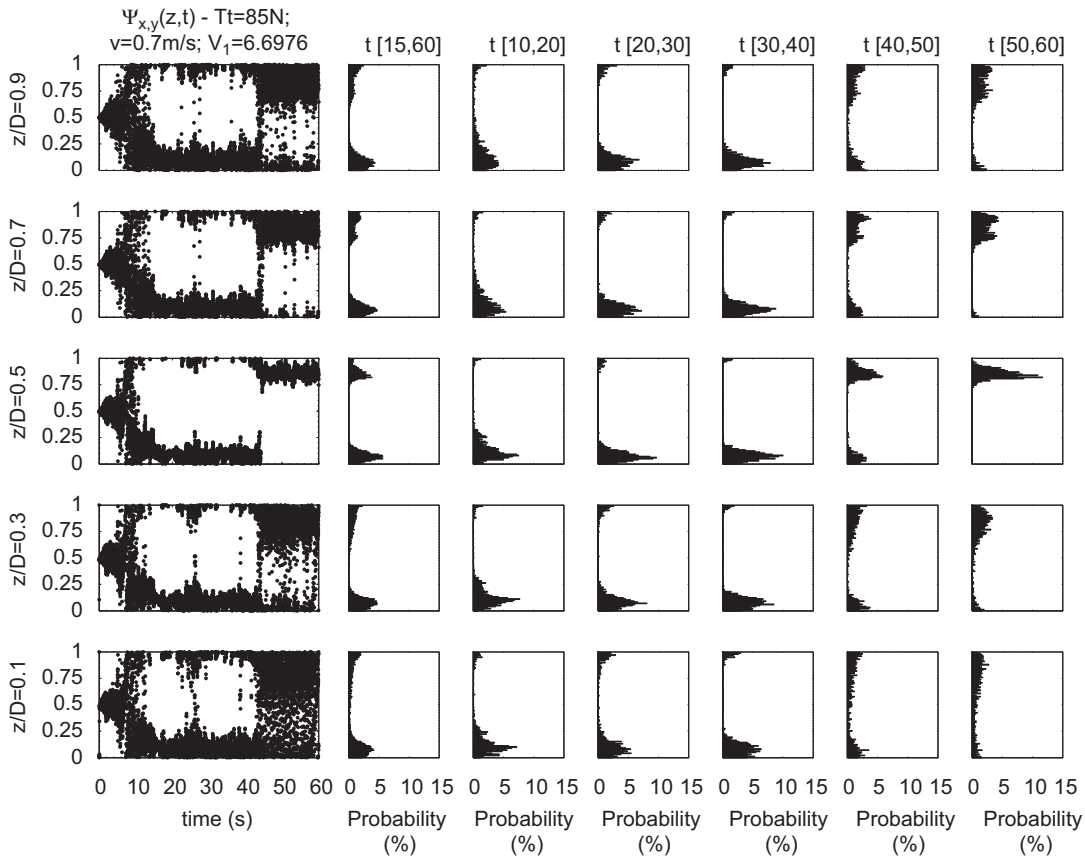

Fig. 16. Example of test: $V = 0.70\,\mathrm{m/s}$, $T_t = 85\,\mathrm{N}$, $\mathrm{Re} = 9800$, $V_1 = 6.7$. In the first column the time series of the cyclic phase difference $\Psi_{x,y}(z_i, t)$ is shown for the whole run. The other five columns show the synchrograms calculated according to the different time intervals.

mode lock-in region shows that synchronisation is incipient with SI of 20%. The values of the phase difference decrease monotonically from about 90° to 45° as the reduced velocity is increased in the initial branch. It remains practically constant in the upper and the lower branches, with values near 30°. Basically as soon as the upper branch is reached, the x–y motions are in phase or almost in phase. For some of the cases in this figure Digital Particle Image Velocimetry (DPIV) was used and the results are shown in Huera-Huarte and Bearman (2009).

4. Discussion

Fig. 18 shows the present data for in-line and cross-flow amplitudes versus reduced velocity, together with other researchers' sets of data in which x–y motion was allowed. In Jauvtis and Williamson (2004) the effect of having two degrees of freedom for different mass–damping combinations was analysed and in the figure cross-flow and in-line amplitude data are shown for two mass ratios, 2.6 and 7. Also, data obtained in the Delta Flume test by Chaplin et al. (2005a) is shown. In that experiment the response was strongly multi-modal and in the figure one can only see the response lock-in regions of the two first modes ($V_1 < 16$) plus four points corresponding to the third mode lock-in region ($V_1 > 16$). A later set of results showing x–y data appears in Sanchis et al. (2008), which is also shown in this figure. Regarding the cross-flow amplitudes, all sets show very similar behaviour in the initial branch. The amplitudes reached in the upper branch reported by Sanchis et al. (2008) and Jauvtis and Williamson (2004) for $m^* = 7$ and Chaplin et al. (2005a) are about 50% larger than the ones in the present work. The amplitudes shown by Jauvtis and Williamson (2004) for $m^* = 2.6$ in the super-upper branch, are slightly over twice the present values. In the lower plot,

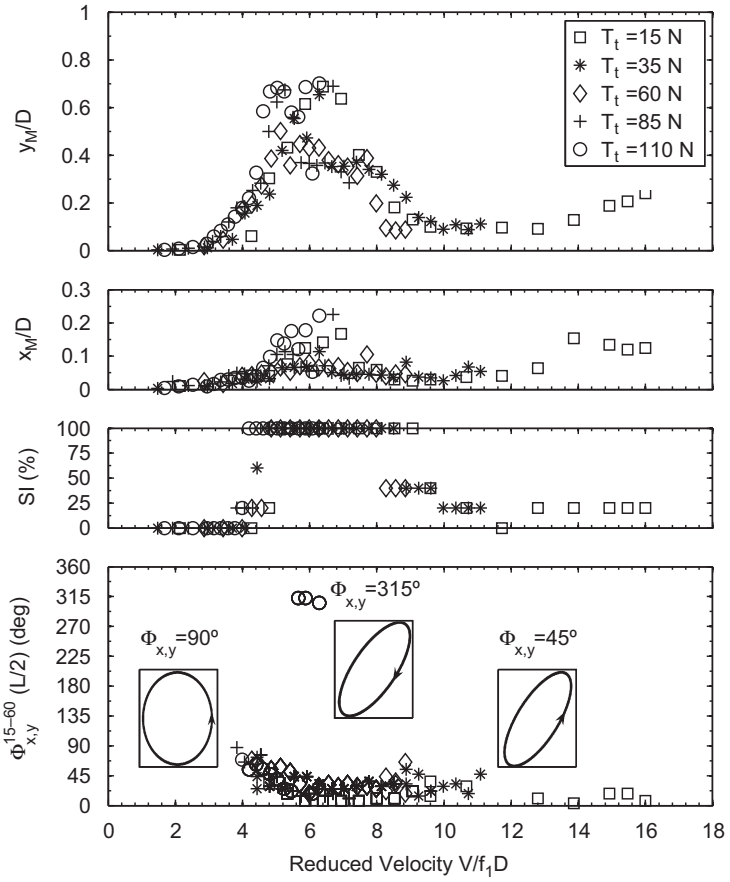

Fig. 17. Non-dimensional amplitudes and phase synchronisation. Upper first and second plots show the maximum non-dimensional cross-flow (y_M/D) and in-line (x_M/D) amplitudes, respectively. The lower plots show the synchronisation index and the phase difference at the mid point of the cylinder model in the time interval Δt_{15}.

the larger in-line amplitudes come from the Delta Flume set of data with values up to 0.4 diameters and from Jauvtis and Williamson (2004) for $m^* = 2.6$, exhibiting amplitudes of about 0.3 diameters, 45% larger than the largest ones in the present work. Regarding these data sets it appears that for high aspect ratio flexible cylinders not only the mass–damping parameter is very important for the response, but also the modal characteristics leading to a certain responding mode which is governed by the applied top tension and hence the natural frequencies. As the top tension is increased for high aspect ratio flexible circular cylinders the less similar the response is to that of flexibly mounted rigid bodies with the same mass–damping values. If tension dominates the structure, the behaviour is that of a cable with low flexural stiffness able to respond multi-modally, otherwise a high aspect ratio cylinder running at low modes responds qualitatively as a rigid body in x–y motion, but with limited amplitudes. The amplitudes in long flexible cylinders are self-limiting as the structure is inherently inextensible and its end points are fixed in space, hence larger amplitudes are limited.

One of the key questions in VIV is to what extent can the maximum attainable amplitudes be predicted as a function of the mass–damping parameter of a body. The first attempt to answer this very basic question was a compilation of data from several researchers resulting in what is traditionally called the Griffin plot (Griffin et al., 1975). Fig. 19 shows a compilation of data obtained under very different conditions plus the data obtained in the present work. Data obtained by Jauvtis and Williamson (2004) comes from experiments on a rigid cylinder in $x - y$ motion. The data from the Delta Flume (Chaplin et al., 2005a) as presented in Huera-Huarte (2006) for the different responding modes, is also included in the figure. The rest of the data presented corresponds to y only motion studies. The collapse of all the data into two clear distinct branches is evident, the lower and the upper branches. The amplitudes of the super-upper branch are only attained from experiments with mass ratios below 6 and some of the modes in the high aspect ratio experiments

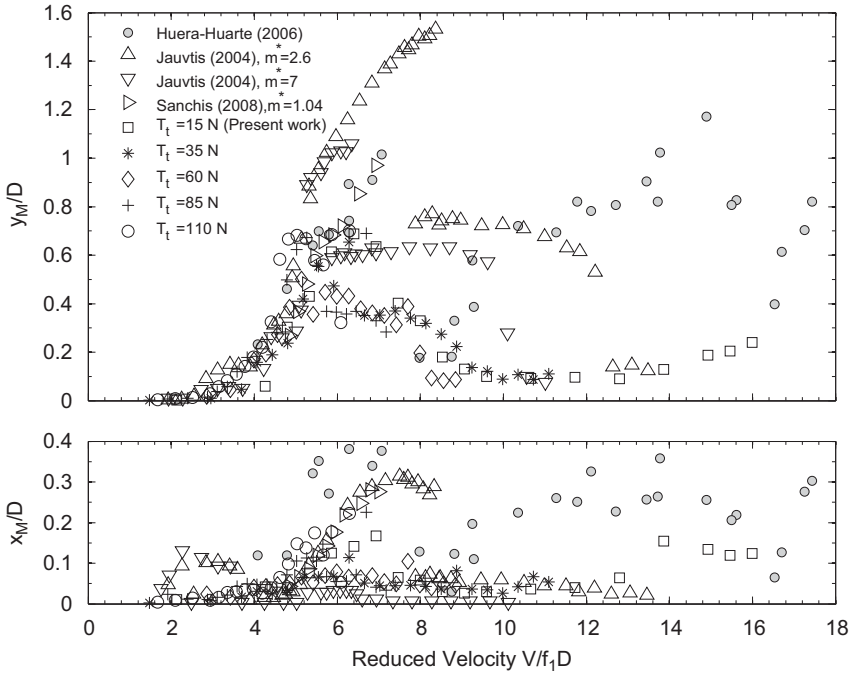

Fig. 18. Cross-flow and in-line maximum amplitudes as a function of reduced velocity. Present work data (□, ◇, ✻, +, ○) against flexible cylinder and two degree of freedom experiments: •—Delta Flume test campaign in Chaplin et al. (2005a) as in Huera-Huarte (2006); △—$m^* = 2.6$ in Jauvtis and Williamson (2004); ▽—$m^* = 7$ in Jauvtis and Williamson (2004); ▷—$m^* = 1.04$ Sanchis et al. (2008).

of the Delta Flume. The equation $y_M/D = (1 - 1.12\alpha + 0.3\alpha^2)\log(0.41\mathrm{Re}^{0.36})$, represented with dashed lines, accounts for the effect of the Reynolds number in the amplitudes as a function of the combined mass–damping parameter (α) as introduced by Govardhan and Williamson (2006).

5. Conclusions

The response of a single long flexible circular cylinder, pin-jointed at its ends and responding in its first structural mode, has been studied. When the lowest tensions are applied to the model, its dynamic response is very similar to that typical of rigid bodies, with clearly defined initial, lower and upper branches of response. As the tension is increased, it starts to behave like a cable, or a tension dominated structure, and the lower branch disappears so all the response is concentrated in the initial and the upper branches. In-line motions are strongly coupled to the cross-flow motion, they increase and decrease at the same reduced velocities as the cross-flow motion. Amplitudes of about 0.7 diameters cross-flow and 0.3 diameters in-line have been observed. This is in contrast to what other researchers have recently demonstrated in two degrees of freedom flexibly mounted rigid body experiments, with mass ratios below 6 (Jauvtis and Williamson, 2004), where amplitudes over 1.5 diameters were related to a new vortex structure consisting of two pairs of three vortices (2 T). Even though some similarities between the dynamic response of rigid and long flexible cylinders exist, it has been shown here how there are important differences, especially regarding the maximum attainable amplitudes caused by the intrinsic nature of the body and its capacity to vibrate at high mode numbers. This observation can obviously have direct implications in offshore riser design codes.

Responding frequencies under lock-in conditions are practically equal to that of the natural frequency of the responding mode, and they can be predicted using a Strouhal number of about 0.16, as other researchers reported in the past (Chaplin et al., 2005a). Synchronisation between in-line and cross-flow motion is only observed under lock-in conditions with phase differences decreasing in the initial branch from values of about 90° to less than 45° inside the upper and lower branches.

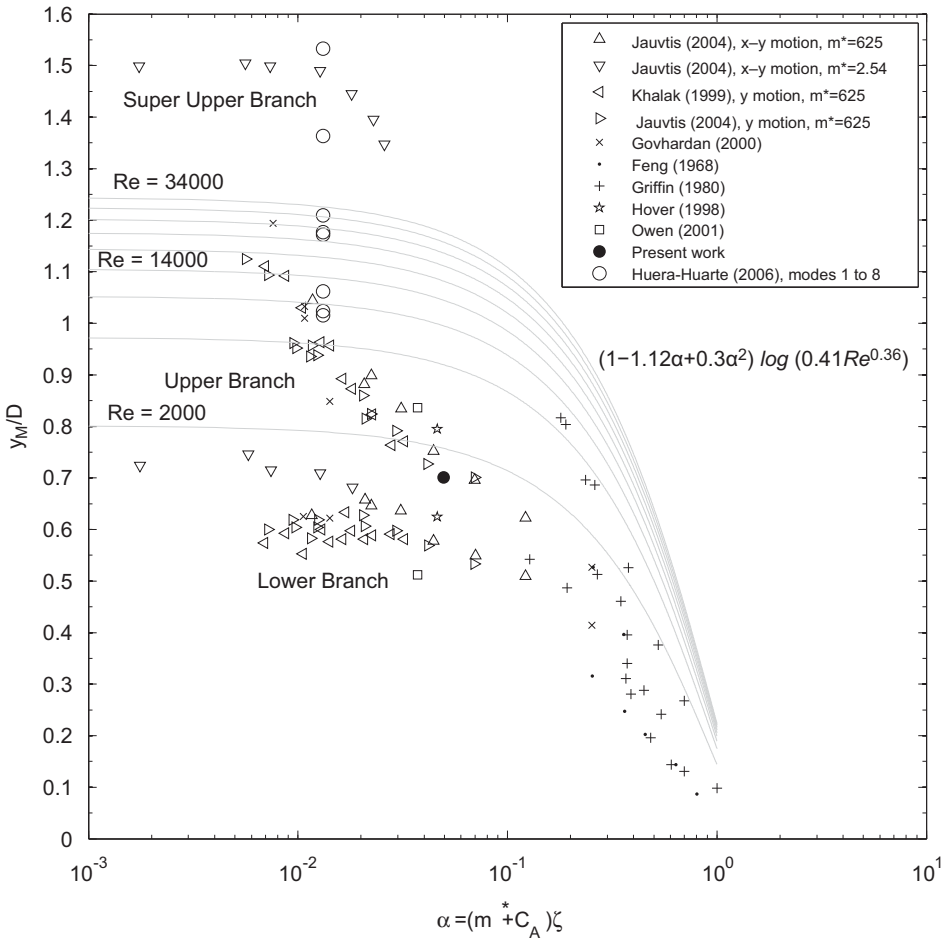

Fig. 19. Maxima of cross-flow displacements (y_M/D) versus reduced mass–damping ($\alpha = (m^* + C_A)\xi$) parameter. •—Present work data; △—'moderate' m^* x–y motion Jauvtis and Williamson (2004); ▽—'low' m^* x–y motion Jauvtis and Williamson (2004); ▷—'moderate' m^* y motion Jauvtis and Williamson (2004); ◁ —'moderate' m^* y motion Khalak and Williamson (1999); ×—Govardhan and Williamson (2006); ⋆—Hover et al. (1998); ·—Feng (1968); +—Griffin (1980); □—Owen et al. (2001); ○—modes 1–8 from Huera-Huarte (2006). Solid lines given by equation $(1 - 1.12\alpha + 0.3\alpha^2)\log(0.41\mathrm{Re}^{0.36})$ (Govardhan and Williamson, 2006) for Reynolds numbers between 2000 and 34 000 with steps of 4000.

Acknowledgements

This work was funded by Universitat Rovira i Virgili through Grant 2006AIRE-03. Special thanks are due to the Department of Aeronautics of Imperial College London.

References

Bearman, P.W., 1984. Vortex shedding from oscillating bluff bodies. Annual Review of Fluid Mechanics 16, 195–222.

Chaplin, J.R., Bearman, P.W., Cheng, Y., Fontaine, E., Graham, J.M.R., Herfjord, K., Huera-Huarte, F.J., Isherwood, M., Lambrakos, K., Larsen, C.M., Meneghini, J.R., Moe, G., Pattenden, R.J., Triantafyllou, M.S., Willden, R.H.J., 2005a. Blind predictions of laboratory measurements of vortex induced vibrations of a tension riser. Journal of Fluids and Structures 21, 25–40.

Chaplin, J.R., Bearman, P.W., Huera-Huarte, F.J., Pattenden, R., 2005b. Laboratory measurements of vortex-induced vibrations of a vertical tension riser in a stepped current. Journal of Fluids and Structures 21, 3–24.

Feng, C.C., 1968. The measurement of vortex-induced effects on flow past stationary and oscillating circular and d-section. M.Sc. Thesis, University of British Columbia Vancouver, B.C., Canada.

Govardhan, R.N., Williamson, C.H.K., 2006. Defining the 'modified griffin plot' in vortex-induced vibration: revealing the effect of reynolds number using controlled damping. Journal of Fluid Mechanics 561, 147–180.

Griffin, O.M., 1980. Vortex-excited cross-flow vibrations of a single cylindrical tube. ASME Journal of Pressure Vessel Technology 102, 158–166.

Griffin, O.M., Skop, R.A., Ramberg, S.E., 1975. The resonant vortex-excited vibrations of structures and cable systems. In: 7th Offshore Technology Conference. Houston, USA, p. OTC 2319.

Hover, F.S., Techet, A.H., Triantafyllou, M.S., 1998. Forces on oscillating uniform and tapered cylinders in crossflow. Journal of Fluid Mechanics 363, 97–114.

Huera-Huarte, F.J., 2006. Multi-mode vortex-induced vibrations of a flexible circular cylinder. Ph.D. Thesis, Imperial College London.

Huera-Huarte, F.J., Bearman, P.W., 2009. Wake structures and vortex-induced vibrations of a long flexible cylinder—Part 2: Drag coefficients and vortex modes. Journal of Fluids and Structures 25(6), this issue, doi:10.1016/j.fluidstructs.2009.03.006.

Jauvtis, N., Williamson, C.H.K., 2003. Vortex-induced vibration of a cylinder with two degrees of freedom. Journal of Fluids and Structures 17, 1035–1042.

Jauvtis, N., Williamson, C.H.K., 2004. The effect of two degrees of freedom on vortex-induced vibration at low mass and damping. Journal of Fluid Mechanics 509, 23–62.

Jeon, D., Gharib, M., 2001. On circular cylinders undergoing two-degree-of-freedom forced motions. Journal of Fluids and Structures 15, 533–541.

Khalak, A., Williamson, C.H.K., 1999. Motions, forces and mode transitions in vortex-induced vibrations at low mass–damping. Journal of Fluids and Structures 13, 813–851.

Lie, H., Kaasen, K.E., 2006. Modal analysis of measures from a large scale viv model test of a riser in linearly sheared flow. Journal of Fluids and Structures 22, 557–575.

Owen, J.C., Bearman, P.W., Szewczyk, A.A., 2001. Passive control of viv with drag reduction. Journal of Fluids and Structures 15, 597–606.

Pikovsky, A., Rosenblum, M., Kurths, J., 2001. Synchronization: a universal concept in nonlinear sciences, first ed. In: Cambridge Nonlinear Science Series.

Sanchis, A., Sælevik, G., Grue, J., 2008. Two-degree-of-freedom vortex-induced vibrations of a spring-mounted rigid cylinder with low mass ratio. Journal of Fluids and Structures, 24, 907–919.

Sarpkaya, T., 2004. A critical review of the intrinsic nature of vortex-induced vibrations. Journal of Fluids and Structures 19, 389–447.

Trim, A.D., Braaten, H., Lie, H., Tognarelli, M.A., 2005. Experimental investigation of vortex-induced vibrations of long marine risers. Journal of Fluids and Structures 21, 335–361.

Vandiver, J.K., Marcollo, H., 2003. High mode number viv experiments. In: IUTAM Symposium on Integrated Modeling of Fully Coupled Fluid–Structure Interactions Using Analysis Computations and Experiments, New Brunswick, NJ, USA. Kluwer, Dordrecht.

Williamson, C., Govardhan, R., 2004. Vortex-induced vibrations. Annual Review of Fluid Mechanics 36, 413–455.

Wooton, L.R., Warner, M.H., Cooper, D.H., 1974. Some aspects of the oscillations of full-scale piles. In: Naudascher, E. (Ed.) Flow-Induced Structural Vibrations. IUTAM-IAHR Symposium Karlsruhe. Springer, Berlin, pp. 587–601.